Auroral boundary correlations between UVI and DMSP

J. F. Carbary, T. Sotirelis, P. T. Newell, and C.-I. Meng
Applied Physics Laboratory, Johns Hopkins University, Laurel, Maryland, USA

Received 12 March 2002; revised 30 September 2002; accepted 4 October 2002; published 15 January 2003.

[1] Equatorward and poleward auroral boundaries from latitude profiles of Polar Ultraviolet Imager (UVI) auroral images were correlated with over 23,000 boundaries derived from 2 years of Defense Meteorological Satellite Program (DMSP) electron precipitation data. Latitude differences between DMSP and UVI boundaries were averaged into 1-hour and 3-hour sectors of magnetic local time (MLT). The statistical distributions of these differences generally peak near zero but have Gaussian-like shapes with widths of about 3°–4° in magnetic latitude. The mean values of these offsets exhibit systematic trends in MLT, with the largest disagreement near 05 MLT for the poleward boundaries and near noon for the equatorward boundaries. The mean offsets were fit to second-order harmonic expansions, which approximately "calibrate" image boundaries with respect to the precipitating electron boundaries. The harmonic fits suggest that the images can yield approximate precipitation boundaries for such purposes as estimating the area of the polar cap. *INDEX TERMS:* 2407 Ionosphere: Auroral ionosphere (2704); 2455 Ionosphere: Particle precipitation; 2494 Ionosphere: Instruments and techniques; 2704 Magnetospheric Physics: Auroral phenomena (2407); *KEYWORDS:* aurora boundaries, electron precipitation

Citation: Carbary, J. F., T. Sotirelis, P. T. Newell, and C.-I. Meng, Auroral boundary correlations between UVI and DMSP, *J. Geophys. Res.*, *108*(A1), 1018, doi:10.1029/2002JA009378, 2003.

1. Introduction

[2] The poleward and equatorward boundaries of the aurora represent important geophysical limits having implications for the ionosphere, the magnetosphere, and their connections to the solar wind. Auroral boundaries can be defined using various methods including all-sky cameras [*Feldstein*, 1963; *Feldstein and Galperin*, 1985], magnetometers [*Ijima and Potemra*, 1978], satellite imagers [*Lui et al.*, 1975], and precipitating particle detectors [*Hardy et al.*, 1985]. Although occasionally subject to controversy, the precise delineation of aurora boundaries has largely become the province of the particle detectors, which, of course, can sample only a tiny portion of the aurora at one instant. Very high altitude auroral imagers on satellites, which have a global field of view, can offer a more expanded and altogether more salubrious picture of the oval, although their boundaries may be subject to contention.

[3] A number of authors have attempted delineation of auroral boundaries using satellite imagery. From crude images from the scanning photometer on the Isis-2 satellite, early investigators marked boundaries apparently by inspection of the intensities [*Lui and Anger*, 1973; *Lui et al.*, 1975]. The same technique, applied to Defense Meteorological Satellite Program (DMSP) line scan photographs, provided the first mathematical representation of equatorward and poleward boundaries in terms of a harmonic expansion in magnetic local time (MLT) [*Holzworth and Meng*, 1975]. Thresholding of DE-2 image intensities provided the first quantitative definition of auroral boundaries, which were tracked during substorms [*Craven and Frank*, 1985, 1987]. A similar thresholding approach has been applied to Polar Ultraviolet Imager (UVI) images to show how polar cap area, as defined by the boundaries of the oval, can change during auroral substorms [*Brittnacher et al.*, 1999].

[4] A natural extension of these efforts has been recent interest in actually correlating image and particle boundaries. *Kauristie et al.* [1999] deduced equatorward and poleward boundaries of the oval using the half widths of the peak intensity from latitude profiles of the Viking UVI images. Correlating a small number of image boundaries and DMSP particle boundaries, they discovered particle boundaries often lay >2° higher in latitude than the image boundaries, especially in the midnight and morning sectors. *Baker et al.* [2000] determined the poleward oval boundaries from Polar UVI images using both the threshold method and a ratio method (the ratio method uses the ratio of intensity to the local time maximum of intensity). The investigation concluded that the ratio method worked better and also identified a systematic difference of about 1° between the DMSP and UVI boundaries in the evening sector where most of the DMSP–UVI matches occurred.

[5] The systematic difference implied by the Kauristie and Baker investigations can be exploited to approximately calibrate the image boundaries using the particle boundaries. One can use this systematic difference to correct the image boundaries and determine the auroral boundaries. To overcome any possible statistical bias caused by a small data set, this investigation uses 2 years worth of DMSP–

0148-0227/03/2002JA009378$09.00

UVI boundaries and over 23,000 matches to provide such a calibration.

2. Data Sets

[6] This investigation merges two data sets. The first data set derives from the auroral images obtained using the Lyman–Birge–Hopfield "long" (LBHL) filter of the UVI on the Polar satellite [*Torr et al.*, 1995]. Auroral radiance in this wavelength band originates from N_2 emissions at altitudes of ~120 km and is considered to be proportional to energy flux of precipitating electrons [e.g., *Germany et al.*, 1998]. The imager provides one image every 18 or 36 s with a resolution of ~30 km at the N_2 emission altitude. The Polar satellite has a highly elliptical orbit of 2×9 R_E so that it views the north polar region for about 9 hours out of every 18-hour orbit. The Polar satellite suffers from an unfortunate "wobble" along one axis of the its 200×228 pixel array so that the resolution in that dimension effectively exceeds ~100 km [*Frank et al.*, 1998]. This wobble introduces a random uncertainty that contributes to the overall error budget of the boundary estimate.

[7] The second data set comes from the SSJ/4 electron detectors on the DMSP satellites [*Hardy et al.*, 1984]. These electrostatic detectors respond to precipitating electrons and ions from 32 eV to 30 keV in logarithmic steps and obtain a complete differential energy spectrum in 1 s. The detectors have narrow apertures looking upward toward local zenith, ensuring that only particles in the atmospheric loss cone are observed. The DMSP satellites have Sun-synchronous orbits with altitudes of ~840 km and periods of ~100 min. Combining the satellite motion with the field of view and accumulation time of the detectors gives an effective spatial resolution of ~7 km. *Newell et al.* [1996a, and references therein] provide a detailed review of DMSP and the SSJ/4 detectors.

[8] The auroral boundaries must be determined in terms of precipitating particle fluxes. This investigation utilizes the work of *Newell et al.* [1991, 1996a, 1996b], who defined various auroral boundaries using precipitating particle data from the DMSP satellites. They define the poleward boundary of the auroral oval on the dayside as the open–closed boundary (recognized as the transition from the boundary plasma sheet region to any open region such as the cusp or polar cap) and on the night side by the B6 electron precipitation boundary (the limit of the subvisual drizzle, where the polar rain appears or the particle fluxes drop below certain limits). The equatorward boundary is defined on the dayside by the equatorward limit of the central plasma sheet or the boundary plasma sheet (which ever is lower in latitude) and on the nightside by the B1e or zero-energy boundary (the equatorward appearance of low-energy electrons). *Sotirelis and Newell* [2000] give a complete exposition of these boundaries and how they can be used to effectively define the auroral oval.

3. Fits to Latitude Profiles

[9] The calibration of the auroral oval involves several processing steps. First, DMSP boundaries are extracted from an extensive online database of precipitating particle boundaries [*Sotirelis et al.*, 1998]. These boundaries are given in terms of MLT and magnetic latitude using the altitude-adjusted corrected geomagnetic coordinates (AAGCM) of *Baker and Wing* [1989]. Second, the DMSP boundaries are matched with UVI images obtained within ±3 min of the DMSP time marks. The intensities of these images are converted on a pixel-by-pixel basis to AAGCM coordinates at an emission altitude of 120 km. Third, latitude profiles of image intensities are constructed. Each profile is 1 hour (15°) wide in MLT, centered on the MLT of DMSP boundary measurement, and averaged into 1° bins of magnetic latitude. Figure 1 shows a typical UVI image and the corresponding latitude profile. Latitudes below 50° are not considered.

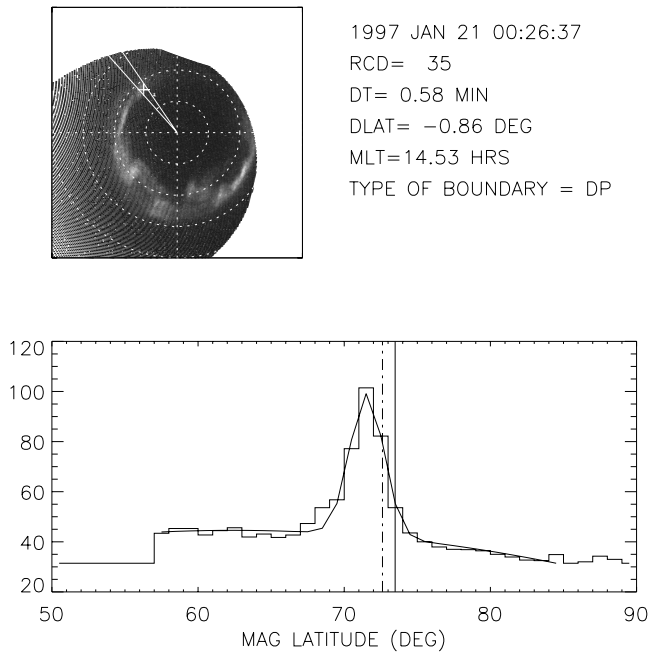

Figure 1. Sample UVI image (top panel) and corresponding latitude profile along the MLT of the DMSP location (bottom panel). The solid lines in the top show the MLT "slice" displayed in the bottom. The bottom histogram represents intensities averaged into a 1-hour MLT sector (centered at 14.5 hours) and 1° latitude bins. The smooth curve represents a fit to a Gaussian plus quadratic background. The solid vertical line denotes the "2FW" boundary of the Gaussian, while the dot-dash vertical line denotes the poleward boundary of the electron precipitation. A dayside poleward (DP) boundary was measured, and the DMSP–UVI difference was −0.86°. See color version of this figure at back of this issue.

[10] Fourth, the binned latitude profiles are then fit to functions having the form of a Gaussian plus a quadratic background:

$$F(\lambda) = A_0 \exp\left[-\frac{1}{2}\left(\frac{\lambda - A_1}{A_2}\right)^2\right] + A_3 + A_4\lambda + A_5\lambda^2 \qquad (1)$$

where λ is the magnetic latitude in degrees, the A_i are coefficients of the fit, and $F(\lambda)$ is the target intensity profile. Admittedly, not all profiles are well fit by (1), but previous authors have noted the similarity of auroral latitude profiles

to Gaussian shapes [e.g., *Eastes et al.*, 2000]. Most profiles are suggestive of such a form, and those which are not are removed by requiring that the fractional standard deviation of the fit be less than 0.20. The Gaussian part of (1) represents the auroral oval, and the quadratic background includes extraneous airglow, off-axis radiance, or unwanted nonoval aurora.

[11] The Gaussian peak immediately locates the center of the auroral oval at $\lambda = A_1$ and determines its full-width-at-half-maximum (FWHM) $\Delta\lambda = 2.354 \cdot A_2$. The fifth part of the processing involves the constraints for using the fit to determine auroral boundaries:

$A_0 > 5$	photons/cm^{2}s (absolute intensity constraint)
$A_1 > 50°$	(lower limit to oval location)
$\frac{A_0}{B} > 0.2$	where $B = A_3 + A_4 \cdot A_1 + A_5 \cdot A_1^2$ is the background at the peak
$\Delta\lambda > 1°$	(Gaussian width must exceed bin resolution)
$\Delta\lambda < 0.3\ (\lambda_{max} - \lambda_{min})$	(Gaussian width must be less than 30% of the range of available bin latitudes reporting finite intensities)

A final criterion is that the fractional standard deviation of the fit must be less than 0.20, as mentioned previously. If these criteria are not satisfied, the UVI–DMSP match is rejected. If these criteria are satisfied, the match is accepted and the oval boundaries are determined by:

$$\lambda_{EQ} = A_1 - \Delta\lambda$$
$$\lambda_{PO} = A_1 + \Delta\lambda \quad (2)$$

These boundaries correspond not to FWHM of the Gaussian, but to twice the FWHM. On a statistical basis, one finds that these "2FW" boundaries represent a near-optimum correlation with the DMSP boundaries. The lower panel of Figure 1 exhibits at sample Gaussian fit for a dayside profile and compares a poleward 2FW boundary with the dayside poleward boundary from precipitating particles.

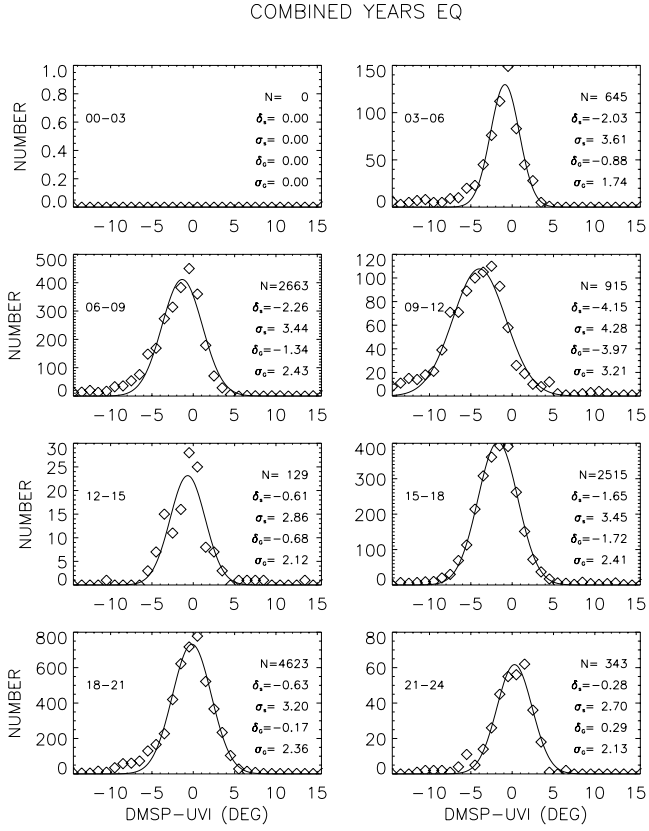

Figure 2. Histograms of DMSP–UVI equatorward boundary differences in 3-hour MLT sectors for 1997–1998. The diamonds represent the numbers of differences in 1° bins, and the solid curves represent Gaussian statistical fits. N is the number of DMSP/UVI matches in the MLT sector; δ_s and σ_s refer the sample mean differences and standard deviations; δ_G and σ_G refer to the Gaussian centers and widths. See text for explanations of these parameters.

4. Statistics of Boundary Differences

[12] Two years of DMSP–UVI data were examined. For 1997–1998, there were 11,833 equatorial matches and 11,244 poleward matches (23,077 total). The differences between the DMSP latitudes and the UVI latitudes were not negligible and, indeed, displayed systematic behavior, a finding reported for smaller data sets elsewhere [e.g., *Kauristie et al.*, 1999; *Baker et al.*, 2000]. For each boundary match, the difference between boundary latitudes was computed:

$$\delta = \lambda_{DMSP} - \lambda_{UVI} \quad (3)$$

These differences were placed into 1-hour MLT sectors (fine resolution) and 3-hour MLT sectors (coarse resolution). Within each MLT sector, one can compute a sample average difference δ_s and a sample standard deviation σ_s.

[13] Within an MLT sector, the distributions of these differences can also be examined using histograms with 1° bin sizes. Figures 2 and 3 exhibit such histogram distributions for the equatorward and poleward boundaries for the combined years 1997–1998 at the coarse MLT resolution. Superposed on the histograms are Gaussian fits to the distributions of differences. These fits have the same form as (1) except $A_3 = A_4 = A_5 = 0$. (Do *not* confuse these difference fits with those for the latitude profiles!) The similarity of these distributions to Gaussians (centers λ_G and widths σ_G) suggests the uncertainties of DMSP and UVI differences are random.

[14] Similar histograms and Gaussians can be constructed for the individual years 1997 and 1998, or for individual seasons or months, for either MLT resolution. When such processing is done, only minor differences in the histograms and Gaussians appear; these differences are due to the statistical dilution of the numbers of boundary matches. The DMSP–UVI offsets remain essentially unchanged within the statistical uncertainties throughout the 2 years of this study.

[15] Tables 1 and 2 give the mean offsets δ_s, their standard deviations σ_s, and the number of samples N (i.e., DMSP–UVI boundary matches) in each MLT bin for the equatorward and poleward boundaries. The offsets are given for the coarse and fine MLT resolutions. The last line of

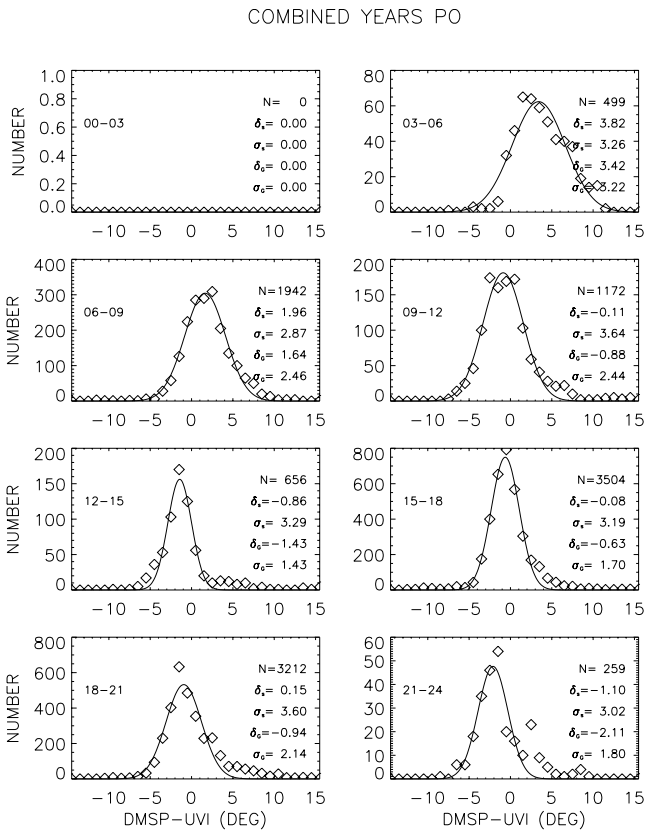

Figure 3. Histograms of DMSP–UVI poleward boundary differences in 3-hour MLT sector for 1997–1998. The format is the same as for Figure 2.

each table gives the offsets and standard deviations averaged over all MLT bins containing samples.

5. Fits to Boundary Differences

[16] In the final step of the analysis, weighted fits were performed to the sample mean differences δ_s. This fit took the form of a low-order harmonic expansion such as that commonly used to describe the auroral oval [e.g., *Holzworth and Meng*, 1975]:

$$\delta_s = F(\varphi) = C_0 + C_1 \cos\varphi + D_1 \sin\varphi + C_2 \cos 2\varphi + D_2 \sin 2\varphi \quad (4)$$

where φ is the angle associated with the MLT and the C and D are coefficients of the fit. Second-order fits (five coefficients)

Table 1. Boundary Correlations for 3-Hour MLT Resolution

	EQ Boundaries			PO Boundaries		
MLT (hours)	δ_s (°)	σ_s (°)	N	δ_s (°)	σ_s (°)	N
00–03	0.00	0.00	0	0.00	0.00	0
03–06	−2.03	3.61	645	3.82	3.26	499
06–09	−2.26	3.44	2663	1.96	2.87	1942
09–12	−4.15	4.28	915	−0.11	3.64	1172
12–15	−0.61	2.86	129	−0.86	3.29	656
15–18	−1.65	3.45	2515	−0.08	3.19	3504
18–21	−0.63	3.20	4623	0.15	3.60	3212
21–24	−0.28	2.70	343	−1.10	3.02	259
0–24	−1.66	3.36	11,833	0.54	3.27	11,244

Table 2. Boundary Correlations for 1-Hour MLT Resolution

	EQ Boundaries			PO Boundaries		
	δ_s (°)	σ_s (°)	N	δ_s (°)	σ_s (°)	N
00–01	0.00	0.00	0	0.00	0.00	0
01–02	0.00	0.00	0	0.00	0.00	0
02–03	0.00	0.00	0	0.00	0.00	0
03–04	0.00	0.00	0	0.00	0.00	0
04–05	0.00	0.00	0	0.00	0.00	0
05–06	−2.03	3.61	645	3.82	3.26	499
06–07	−1.24	2.82	1287	2.55	2.67	685
07–08	−2.56	3.15	859	1.88	2.75	752
08–09	−4.28	4.19	517	1.26	3.11	505
09–10	−4.44	4.06	518	0.31	3.20	607
10–11	−4.26	4.10	302	−0.34	3.25	346
11–12	−2.24	5.39	95	−0.88	4.96	219
12–13	0.02	2.99	47	−0.96	3.29	169
13–14	0.45	3.12	26	−1.27	2.41	235
14–15	−1.63	2.27	56	−0.42	3.91	252
15–16	−2.28	2.67	184	−0.20	2.84	428
16–17	−2.03	2.92	853	−0.36	3.09	1121
17–18	−1.35	3.76	1478	0.11	3.31	1955
18–19	−0.94	3.14	1408	−0.11	3.38	1122
19–20	−0.73	3.16	1690	0.54	3.94	911
20–21	−0.22	3.27	1525	0.08	3.51	1179
21–22	−0.28	2.70	343	−1.10	3.02	259
22–23	0.00	0.00	0	0.00	0.00	0
23–24	0.00	0.00	0	0.00	0.00	0
0–24	−1.77	3.37	11,833	0.29	3.29	11,244

were performed. Fits of this order allowed sufficiently detailed characterization of the differences without introducing extraneous wiggles. The fits were weighted by the numbers of matches in MLT sectors. (Weighting by the standard deviations of the bin averages tended to produce unphysical fits, especially for the equatorward boundaries.)

[17] Figure 4 displays these fits for equatorward and poleward boundaries for both the fine and coarse MLT sectorizations. Systematic differences between DMSP boundaries and UVI boundaries are readily apparent. Again, these systematic differences are similar for either year, any season or month, and for at both MLT resolutions. Coefficients for these fits appear in Table 3; use of these coefficients in (4) will generate δ_s in degrees. The σ_{FIT} in the table represents the weighted standard deviations of the harmonic fits, while N indicates the number of DMSP–UVI matches used. Because of the DMSP orbits, no boundary matches were found at MLTs from 2300 to 0500 hours. Also, a relatively small number of matches were found for the equatorial boundaries from 1200 to 1500 hours; these received a low fitting weights and did not attract the harmonic curves in the equatorial panels of Figure 4.

[18] To more readily illustrate the DMSP–UVI differences, the offsets of Figure 4 are shown on a more familiar polar display in Figure 5. Hypothetical UVI boundaries are shown as dashed line circles at 60° (equatorward) and 70° (poleward) magnetic latitude, while the DMSP boundaries would appear as the diamond symbols and solid lines. The standard deviations appear as radial segments plotted across the diamonds.

6. Discussion

[19] Figures 4 and 5 and Tables 1, 2, and 3 exhibit the principal results of the DMSP–UVI boundary analysis. The poleward differences have the same general shape for

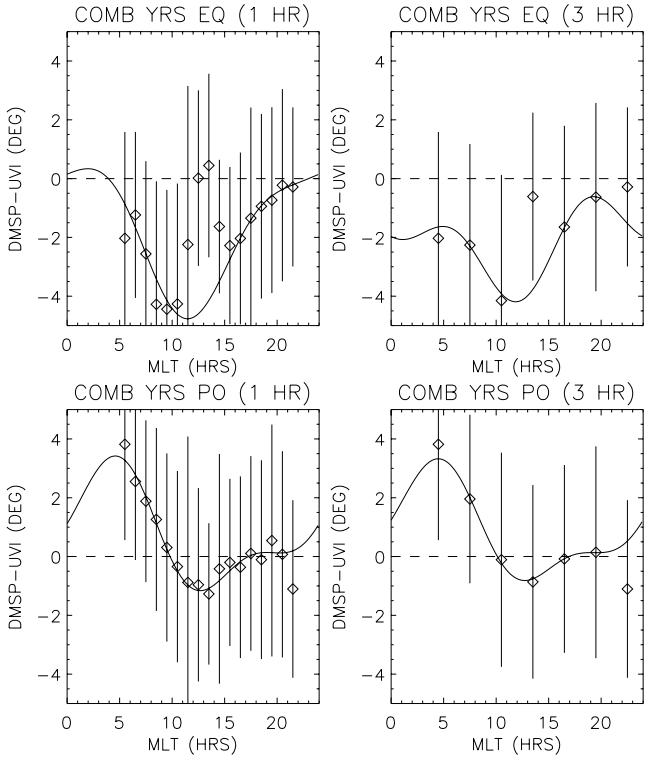

Figure 4. Fits to systematic boundary differences for 1997–1998. Diamond symbols indicate the centers (means) of the Gaussian statistical fits to DMSP–UVI differences: for 1-hour (left panels) and 3-hour (right panels) MLT bins. The vertical bars represent the widths of the Gaussians. The solid curves represent second-order (five-term) harmonic fits. These fits have been weighted by the number of boundary matches in an MLT sector. Equatorward boundary matches appear in the top panels, while poleward boundary matches appear in the bottom panels.

each year, each season of the year, and each MLT resolution. The poleward boundary differences remain near $-1°$ from 0800 to 2200 hours, but then begin a systematic increase as MLTs decrease from 0700 hours. The poleward fits suggest particle boundaries differ significantly from the imager boundaries in the postmidnight sector, although no precipitating particle data are available to directly verify this.

[20] The equatorward boundary differences are also essentially the same throughout the 1997–1998 time period but differ from the poleward boundary differences. The equatorward differences are near zero for MLTs after 1700 hours, but exhibit a systematic dip between 0600 and 1700

Table 3. Harmonic Coefficients for 1997–1998 Boundaries

	EQ (1 hour)	EQ (3 hours)	PO (1 hour)	PO (3 hours)
C_0	−1.74	−2.19	0.80	0.89
C_1	2.44	1.11	1.11	1.09
D_1	−0.05	−0.45	1.48	1.43
C_2	−0.54	−0.89	−0.79	−0.65
D_2	0.30	−0.14	0.38	0.39
σ_{FIT}	0.10	0.06	0.06	0.05
N	11,833		11,244	

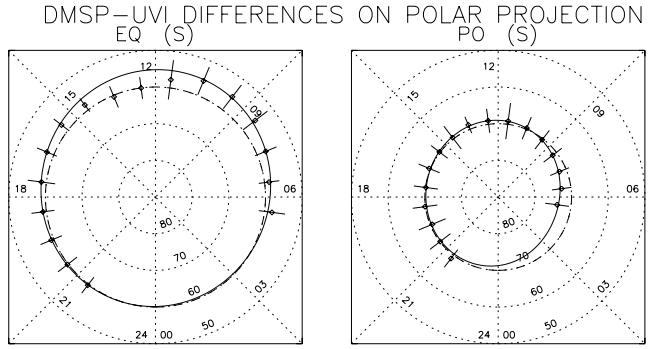

Figure 5. Hypothetical UVI boundaries (dashed-line circles) compared to DMSP boundary (diamond symbols) found by using the Gaussian offsets and widths (see Figures 2 and 3). The solid lines indicate the adjusted boundary obtained from the harmonic fit to the offsets ((4) and Table 1). The UVI equatorward boundary was assumed to be a circle at 60° magnetic latitude, while the poleward boundary was assumed to be a circle at 70°.

hours. The fits suggest the equatorward differences are near zero in the midnight and postmidnight sector. Peculiarly, between 1200 and 1400 hours, a significant departure from the curve fits exists for both 1997 and 1998. This difference occurs in a relatively small number of boundary matches, so it is not emphasized in the weighted fits. The departure may represent merely a statistical anomaly, peculiarly seen in both years. Alternately, the peak may be real, possibly a remnant of improperly recognized cusp signatures in the UVI boundary fits.

[21] The fits to the boundary differences effectively provide a "calibration" of the UVI–LBHL boundaries in terms of precipitating particle boundaries. For any given MLT, a UVI–LBHL boundary can be "corrected" using the functional form (4) and the coefficients in Table 3. An example of the use of this corrections appears in the next section.

[22] Unfortunately, this calibration involves some rather large uncertainties in the offsets. The standard deviations of 3°–4° often exceed the offsets themselves, suggesting that the corrections are unnecessary or even that no meaningful relation exists between the DMSP and UVI boundaries. Three important considerations mitigate against this interpretation. First, the offset distributions (Figures 2 and 3) are well represented by monomodal Gaussians, which implies the uncertainties are random and the mean is therefore a representative value of the distribution. Second, although the standard deviations are large, the uncertainties in the mean values are very small because of the large number of samples. That is, $\sigma_{mean} = \sigma_s/\sqrt{N} < 0.4°$, because $\sigma_s \approx 4°$ (or less) and $N > 100$ [e.g., *Bevington*, 1969]. Third, the arrangement of the mean offsets in MLT is not random but systematic. Indeed, the offsets are well represented as a harmonic function of MLT.

7. Example: Determining Polar Cap Area

[23] As an example of the use of the oval calibration, consider determining the polar cap area A from the boundaries in a UVI image. Given the UVI boundaries $\lambda_{UVI}(\varphi_i)$

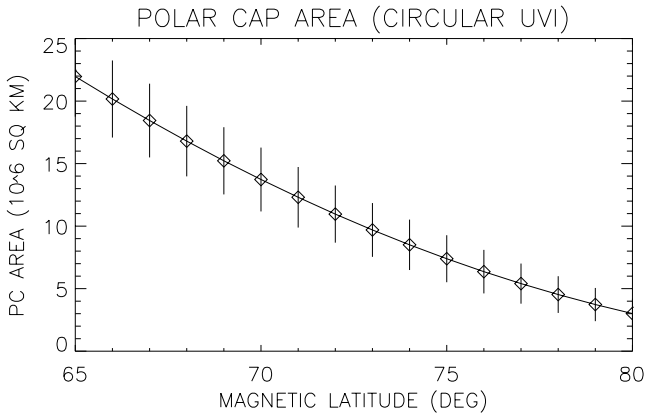

Figure 6. Polar cap areas and area uncertainties assuming circular UVI boundaries at various magnetic latitudes. The circular UVI boundaries are converted into precipitating particle (DMSP) boundaries, and the areas and their uncertainties are computed using (5) and (6).

at discrete local times φ_i, the precipitating particle boundaries $\lambda_{DMSP}(\varphi_i)$ are obtained from (4):

$$\lambda_{DMSP}(\varphi_i) = \lambda_{UVI}(\varphi_i) + F(\varphi_i)$$

The harmonic expansion $F(\varphi_i)$ will use the polarward set of C and D coefficients from Table 1. Then the polar cap area is:

$$\begin{aligned} A &= r^2 \int_0^{24h} \int_{\lambda_{DMSP}}^{90^\circ} \cos\lambda d\lambda d\delta = r^2 \int_0^{24h} [1 - \sin\lambda_{DMSP}(\varphi)] d\varphi \\ &\approx \frac{2\pi r^2}{24} \sum_{i=1}^{24h} [1 - \sin\lambda_{DMSP}(\varphi_i)] \\ &= \frac{2\pi r^2}{24} \sum_{i=1}^{24h} [1 - \sin(\lambda_{UVI}(\varphi_i) + F(\varphi_i))] \end{aligned} \quad (5)$$

where r is the polar radius of the Earth at auroral altitudes (≈6476 km) and the summation runs over all local times in increments of 1 hour (=2π/24). (A spherical geometry is used.) The angles within the sum are φ_i = (0.5, 1.5, 2.5,...23.5) · (2π/24), which are converted from hours to radians for numerical calculations.

[24] The formal uncertainty in A is:

$$\begin{aligned} \sigma_A &= \sqrt{\left(\frac{\partial A}{\partial \lambda}\right)^2 \sigma_\lambda^2 + \left(\frac{\partial A}{\partial F}\right)^2 \sigma_F^2 + \left(\frac{\partial A}{\partial \lambda}\right)\left(\frac{\partial A}{\partial F}\right)\sigma_{\lambda F}^2} \\ &\approx \left[\frac{2\pi r^2}{24} \sum_i \cos(\lambda_{UVI}(\varphi_i) + F(\varphi_i))\right] \sqrt{\sigma_\lambda^2 + \sigma_F^2} \end{aligned} \quad (6)$$

Uncertainties in r have been ignored, and λ and F are assumed to be uncorrelated, which makes $\sigma_{\lambda F}^2 = 0$. The uncertainty σ_λ in the UVI boundary is ∼3.5° (from Tables 1 and 2) and the uncertainty σ_{FIT} in F is ∼0.1° (from Table 3).

[25] Using (5) and (6), calculations of the polar cap area and its uncertainty were calculated assuming hypothetical circular boundaries (that is, $\lambda_{UVI}(\varphi)$ = constant magnetic latitude). Figure 6 displays the resulting polar cap areas and their uncertainties as functions of the magnetic latitude of such circular boundaries. The uncertainty decreases with increasing latitude, although the fractional uncertainty σ_A/A increases from 0.29 at 65° to 0.79 at 80°.

8. Conclusions

[26] A new method for finding auroral boundaries fits a Gaussian plus background to latitudinal intensity profiles taken from UVI–LBHL images. The goodness of this fit determines the reliability of the boundaries, which are then matched with precipitating electron boundaries obtained from DMSP satellites. The differences, or offsets, between DMSP and UVI boundaries are placed in MLT bins and examined on a statistical basis. Although the differences are generally near zero, systematic offsets of up to 4° appear between the DMSP and UVI boundaries. The offsets remain constant within statistical uncertainties of about ±3.5° for both years studied. The offset is greatest for the equatorward boundaries near local noon and for the poleward boundaries near 0400 hours. Fitting the offsets to a second-order harmonic expansion converts UVI boundaries to the precipitating particle boundaries, at least to within the statistical limits. This conversion can be used, for example, to calculate the polar cap area from satellite images.

[27] **Acknowledgments.** The authors wish to thank Fred Rich and the U.S. Air Force for providing DMSP particle data and George Parks and the UVI team for providing UVI image data. This research was supported by AFOSR grant F49620-00-1-0172.

References

Baker, J. B., C. R. Clauer, A. J. Ridley, V. O. Papitashvili, M. J. Brittnacher, and P. T. Newell, The nightside poleward boundary of the auroral oval as seen by DMSP and the Ultraviolet Imager, *J. Geophys. Res.*, *105*, 21,267–21,280, 2000.

Baker, K. B., and S. Wing, A new magnetic coordinate system for conjugate studies at high latitudes, *J. Geophys. Res.*, *94*, 9139–9143, 1989.

Bevington, P. R., *Data Reduction and Error Analysis for the Physical Sciences*, chapters 2, 5, McGraw-Hill, New York, 1969.

Brittnacher, M., M. Fillingim, G. Parks, G. Germany, and J. Spann, Polar cap area and boundary motion during substorms, *J. Geophys. Res.*, *104*, 12,251–12,262, 1999.

Craven, J. D., and L. A. Frank, The temporal evolution of a small auroral substorm as viewed from high altitudes with Dynamics Explorer 1, *Geophys. Res. Lett.*, *12*, 465–468, 1985.

Craven, J. D., and L. A. Frank, Latitudinal motions of the aurora during substorms, *J. Geophys. Res.*, *92*, 4565–4573, 1987.

Eastes, R. W., R. E. Daniell Jr., and F. J. LeBlanc, Coincident ultraviolet imager and energetic particle sensor observations of the continuous electron aurora, *J. Atmos. Sol. Terr. Phys.*, *61*, 927–934, 2000.

Feldstein, Y. I., On the morphology of auroral and magnetic disturbances at high latitudes, *Geomagn. Aeron.*, *3*, 183, 1963.

Feldstein, Y. I., and Y. I. Galperin, The auroral luminosity structure in the high-latitude upper atmosphere: Its dynamics and relationship to the large-scale structure of the Earth's magnetosphere, *Rev. Geophys.*, *23*, 217–275, 1985.

Frank, L. A., J. B. Sigwarth, and W. R. Paterson, High-resolution global images of Earth's auroras during substorms, in *Substorms-4*, edited by S. Kokubun and Y. Kamide, pp. 3–8, Kluwer Acad., Norwell, Mass., 1998.

Germany, G. A., J. F. Spann, G. K. Parks, M. J. Brittnacher, R. Elsen, L. Chen, D. Lummerzheim, and M. H. Rees, Auroral observations from the POLAR Ultraviolet Imager (UVI), in *Geospace Mass and Energy Flow, Geophys. Monogr.*, vol. 104, edited by J. L. Horwitz, D. L. Gallagher, and W. K. Peterson, pp. 149–160, AGU, Washington, D. C., 1998.

Hardy, D. A., L. K. Schmitt, M. S. Gussenhoven, F. J. Marshall, H. C. Yeh, T. L. Shumaker, A. Hube, and J. Pantazis, Precipitating electron and ion detectors (SSJ/4) for the block 5D/flights 6–10 DMSP satellites: Calibration and data presentation, *Rep. AFGL-TR-84-0317*, Air Force Geophys. Lab., Hanscom AFB, Mass., 1984.

Hardy, D. A., M. S. Gussenhoven, and E. Holman, A statistical model of auroral electron precipitation, *J. Geophys. Res.*, *90*, 4229–4248, 1985.

Holzworth, R. H., and C.-I. Meng, Mathematical representation of the auroral oval, *Geophys. Res. Lett.*, *2*, 377–380, 1975.

Iijima, T., and T. A. Potemra, Large-scale characteristics of field-aligned currents associated with substorms, *J. Geophys. Res.*, *83*, 599–615, 1978.

Kauristie, K., J. Weygand, T. I. Pulkkinen, J. S. Murphree, and P. T. Newell, Size of the auroral oval: UV ovals and precipitation boundaries compared, *J. Geophys. Res.*, *104*, 2321–2331, 1999.

Lui, A. T. Y., and C. D. Anger, A uniform belt of diffuse aurora emission seen by the Isis-2 scanning photometers, *Planet. Space Sci.*, *21*, 799–809, 1973.

Lui, A. T. Y., C. D. Anger, and S.-I. Akasofu, The equatorward boundary of the diffuse aurora and auroral substorms as seen by the Isis-2 auroral scanning photometer, *J. Geophys. Res.*, *80*, 3603–3614, 1975.

Newell, P. T., S. Wing, C.-I. Meng, and V. Sigillito, The auroral oval position, structure, and intensity of precipitation from 1984 onward: An automated on-line data base, *J. Geophys. Res.*, *96*, 5877–5882, 1991.

Newell, P. T., Y. I. Feldstein, Y. I. Galperin, and C.-I. Meng, Morphology of nightside precipitation, *J. Geophys. Res.*, *101*, 10,737–10,748, 1996a.

Newell, P. T., Y. I. Feldstein, Y. I. Galperin, and C.-I. Meng, Correction to ''Morphology of nightside precipitation'', *J. Geophys. Res.*, *101*, 17,419–17,421, 1996b.

Sotirelis, T., and P. T. Newell, Boundary-oriented electron precipitation model, *J. Geophys. Res.*, *105*, 18,655–18,673, 2000.

Sotirelis, T., P. T. Newell, and C.-I. Meng, Shape of the open–closed boundary of the polar cap as determined from observations of precipitating particles by up to four DMSP satellites, *J. Geophys. Res.*, *103*, 399–406, 1998.

Torr, M. R., et al., A far ultraviolet imager for the international solar–terrestrial physics mission, *Space Sci. Rev.*, *71*, 329–383, 1995.

J. F. Carbary, C.-I. Meng, P. T. Newell, and T. Sotirelis, Applied Physics Laboratory, Johns Hopkins University, Laurel, MD 20723, USA.(james.carbary@jhuapl.edu)

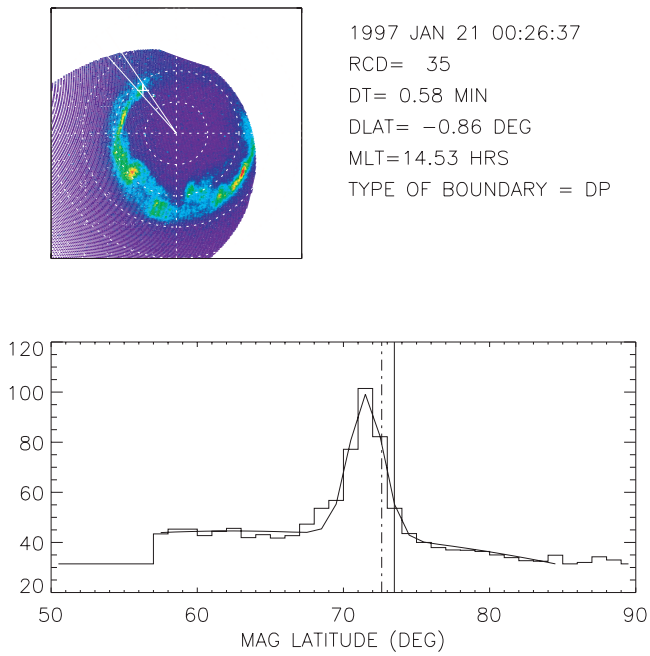

Figure 1. Sample UVI image (top panel) and corresponding latitude profile along the MLT of the DMSP location (bottom panel). The solid lines in the top show the MLT "slice" displayed in the bottom. The bottom histogram represents intensities averaged into a 1-hour MLT sector (centered at 14.5 hours) and 1° latitude bins. The smooth curve represents a fit to a Gaussian plus quadratic background. The solid vertical line denotes the "2FW" boundary of the Gaussian, while the dot-dash vertical line denotes the poleward boundary of the electron precipitation. A dayside poleward (DP) boundary was measured, and the DMSP−UVI difference was −0.86°.